JTTEE5 9:399-406

Thermal Sprayed Nanostructured WC/Co Hardcoatings

B.H. Kear, R.K. Sadangi, M. Jain, R. Yao, Z. Kalman, G. Skandan, and W.E. Mayo

(Submitted 8 October 1999)

Hardcoatings of WC/Co, produced by high-velocity oxy-fuel (HVOF) and air plasma spray (APS) deposition, have been studied. During HVOF deposition, nanostructured powder experiences more decarburization than conventional powder, whereas in APS deposition, just the opposite effect occurs This is explained in terms of the influence of the highly porous, spherical-shell morphology of the nano-WC/Co particles on their melting characteristics and reaction kinetics. In particular, heterogeneous melting and localized superheating of the high-surface-area powder is considered to be a controlling factor in decarburization. The situation is further complicated in APS deposition by high-temperature vaporization of Co and C.

Keywords decarburization, gasification, nanostructures, oxidation

1. Introduction

Materials with fine-scale structures have long been recognized to exhibit remarkable and technologically attractive properties. Over the past decade,[1,2] interest has been growing in a new class of materials that are composed of ultrafine grains or particles. A feature of such *nanostructured* materials is the high fraction of atoms that reside at grain boundaries or interfaces in the materials. Although much of today's R&D activity is focused on the synthesis and processing of nanostructured bulk materials, there is increasing awareness of the potential for nanostructured coatings.[3]

This paper compares the microstructures of WC/Co coatings obtained by thermal spraying of conventional and nanostructured powders, utilizing both high-velocity oxy-fuel (HVOF) and air plasma spray (APS) systems. As will be shown, the microstructures of the coatings are strongly affected by spray parameters and powder-feed characteristics. In particular, the unusual structure and morphology of the chemically synthesized nanostructured powder exerts a strong influence on the resulting coating microstructure.

2. Experimental

Feed powders of conventional WC/15Co and nanostructured WC/12Co were obtained from Surface Engineering & Alloy Co. (St. Petersburg, FL) and Union Miniere Research-North America (formerly Nanodyne Inc., New Brunswick, NJ), respectively. These powders have strikingly different characteristics, which are a consequence of different production methods.

B.H. Kear, R.K. Sadangi, M. Jain, R. Yao, Z. Kalman, G. Skandan, and **W.E. Mayo,** Center for Nanomaterials Research, Rutgers University, Piscataway, NJ 08854-8065. Contact e-mail: bkear@rci.rutgers.edu.

Conventional WC/Co powder is produced by mechanical mixing of WC and Co particles in a fluid medium, spray drying to form solid agglomerates, and heat treating to consolidate the agglomerated particles. Nanostructured WC/Co powder is produced by spray drying an aqueous solution mixture of salts of the constituent elements to develop a homogeneous precursor powder, followed by fluid bed thermochemical conversion (pyrolysis, reduction, and carburization) of that powder to form the desired nano-WC/Co end-product powder.[4,5] During the cool-down cycle, the high-surface-area powder is passivated with oxygen-rich species. Without this precautionary measure, the powder is susceptible to spontaneous combustion when exposed to air.

The as-produced conventional powder consists of solid agglomerates, which are screened to a relatively narrow size distribution, typically within the range of 15 to 40 μm. In contrast, the as-produced nanostructured powder has a highly porous, spherical-shell morphology, and particle size of 5 to 30 μm (Fig. 1). The individual WC grains residing within each nanocomposite particle are about 40 to 50 nm.[5]

Thermal spraying was carried out at A&A Company Inc. (South Plainfield, NJ) using both HVOF and APS torches, operating under the conditions specified in Table 1. Plasma spraying was performed with Metco 9MB and 3MB torches, using both Ar/10 vol.% He and N_2/12 vol.% H_2 as plasma gases. The much longer particle residence time in the hot zone of the N_2/H_2 plasma, resulting from release of recombination energy downstream in the plasma jet, heats the particles to much higher temperatures. Therefore, the trend in thermal spraying, represented by HVOF Ar/He plasma, and N_2/H_2 plasma, reflects a sharp increase in the mean particle temperature achieved during spraying.

Samples of powders and coatings were prepared for optical examination by standard metallographic techniques, and examined in both the as-polished and etched conditions. Of particular interest was the extent of porosity and evidence for decarburization in the coatings. X-ray diffraction analysis was carried out in a Siemens D5000 diffractometer, using Cu K_α radiation (40 kV, 30 mA), and JADE (version 3.1, Materials Data Inc., Livermore, CA) for phase identification. Wet chemical analysis was used for determining composition, and field emission-scanning electron microscopy (FE-SEM) for structural analysis. In addition, Vick-

ers hardness measurements were performed on polished surfaces and cross sections of the coatings, using a microhardness tester (Leco Corp., St. Joseph, MI). At least five indentations were made at each representative location in a sample to obtain an average value.

3. Results and Discussion

3.1 Coatings Produced by HVOF Deposition

The HVOF coatings were produced using both conventional and nanostructured powders, with nominal compositions WC/15Co and WC/12Co, respectively; actual compositions are given in Table 2. Metallographic examination of cross sections of the two types of coatings revealed some striking differences in their microstructures.

In the nanocoating case, a typical coating microstructure consists of adjacent bands of *speckled* and *clear* material, interspersed with interband porosity (Fig. 2). Under high resolution in the SEM, a speckled region of the microstructure was revealed to be a highly porous aggregate of WC and Co particles, (Fig. 3a). In contrast, a clear region of the microstructure (Fig. 3b), was composed of a relatively pore-free, sintered aggregate of WC particles. Close examination of Fig. 3(a) shows very small WC particles (~50 nm) that appear to be in different stages of coalescence to form larger particles (~500 nm); some examples are indicated by arrows in the figure. Such a structure is very similar to that found in the original powder particles. Thus, it may be concluded that in this particular region of the microstructure, and similar ones widely dispersed throughout the coating, the material must have been heated but not necessarily melted. On the other hand, adjacent regions of the microstructure, similar to those shown in Fig. 3 (b), must have undergone melting and consolidation, accompanied by some structural modification by a liquid Co-assisted sintering mechanism, *i.e.*, WC nanoparticle aggregates in Fig. 3(a) appear to have been transformed into denser particles in Fig. 3(b).

Other regions of the microstructure, representative examples of which are shown in Fig. 4, showed evidence for variations in WC particle size, shape, and degree of agglomeration, and associated nanoscale/microscale porosity. For example, the WC volume fraction in Fig. 4 (c) is larger than that in Fig. 4 (b). This is interpreted to mean that the material in Fig. 4(c) must have been exposed to a higher temperature than that in Fig. 4(b), resulting in greater dissolution of the WC particles in the liquid Co phase. Such behavior is in accord with the pseudobinary phase diagram for WC-Co, where a steeply rising liquidus curve occurs on the WC-rich side of the eutectic.[6] As further evidence for this dissolution mechanism, we note that many of the WC particles in Fig. 4(c), indicated by arrows, are rounded in appearance. In other areas of Fig. 4(b), the coarsened WC particles are faceted, which is usually ascribed to good wetting between WC and Co phases.[7] Moreover, we note the misshapen aspect of some of the larger particles, which is indicative of a polycrystalline structure. This is considered to be the result of liquid phase-assisted sintering of porous aggregates of the type shown in Fig. 4(a).

Taken together, these observations provide strong evidence for nonuniform or heterogeneous melting of the porous, shell-like nano-WC/Co particles during spraying. As indicated in Fig. 5, only the liquid phase-sintered part of a heated particle would be expected to yield a dense structure when it impacts the cold

Table 1 Thermal spray parameters

		APS	
Deposition System	**HVOF**	**Ar/He plasma**	**N_2H_2 plasma**
Gun	Metco DJ	Metco 9MB	Metco 3MB
Nozzle	#2 injector: VA Shell: jetted #2 Insert: V4 siphon Plug: V4 air cap	GH	G
Gas type	oxygen/propane/air	Argon/He	N_2/H_2
Gas pressure (Kpa)	689/689/617-551	689/689	344.5/344.5
Gas flow (m^3/h)	16.34/4.98/24.27	. . .	. . .
Amperes	. . .	500	600
Volts	. . .	70–75	70–75
Spray distance (cm)	15–20	7.5	7.5
Spray rate (kg/h)	2.27	3.64	2.275

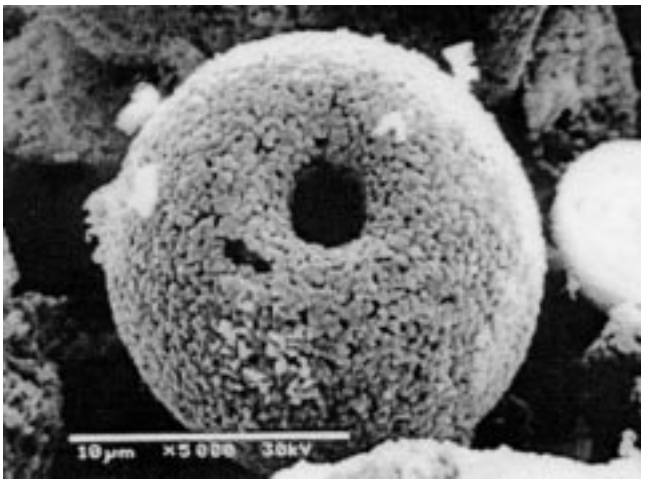

Fig. 1 SEM micrograph of an as-produced nano-WC/12Co powder particle, showing its characteristic porous, spherical-shell morphology

Table 2 Composition of starting powders and coatings

		Composition (wt.%)				
	Material	**W**	**Co**	**Total C**	**Free C**	**O/N (ppm)**
Surface engineering	Starting powder	79.87	14.94	5.19	0.04	1670/480
powder feed	HVOF coating	79.98	15.1	4.85	0.07	5730/460
(WC/15Co)	N_2H_2 plasma coating	98.17	0.55	1.28	0.05	2260/280
Nanostructured	Starting powder	82.63	12	5.37	0.04	1000/200
powder feed	HVOF coating	84.44	11.66	3.9	0.09	1770/140
(WC/12Co)	N_2H_2 plasma coating	92.6	4.76	2.65	0.12	2380/70

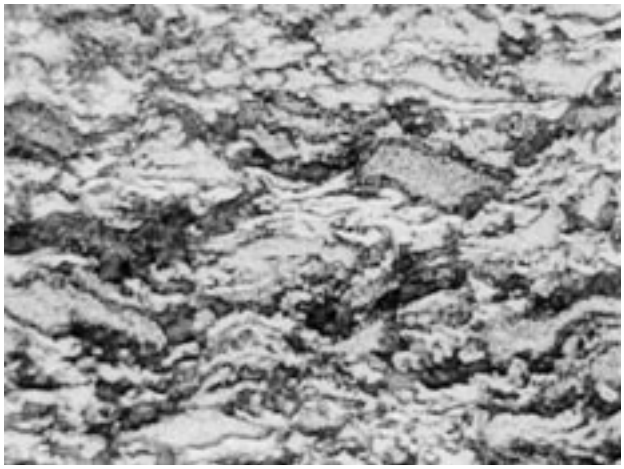

(a)

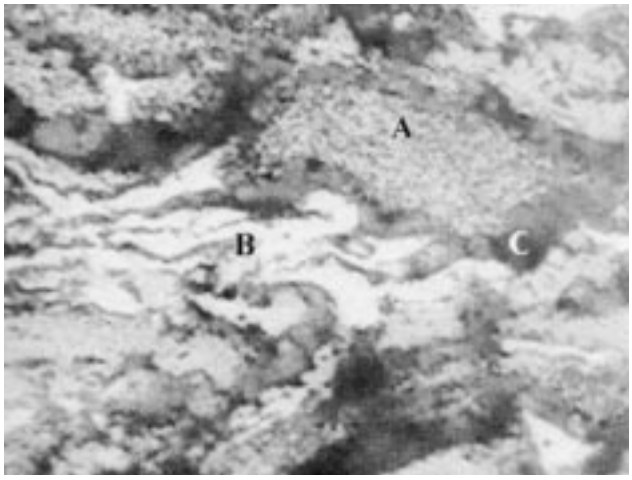

(b)

Fig. 2 Optical micrographs (etched and repolished) of HVOF-sprayed WC/12Co nanocoating: (**a**) low magnification showing "banded" structure of coating and (**b**) same area at higher magnification showing speckled (**A**) and clear (**B**) regions and interband porosity (**C**)

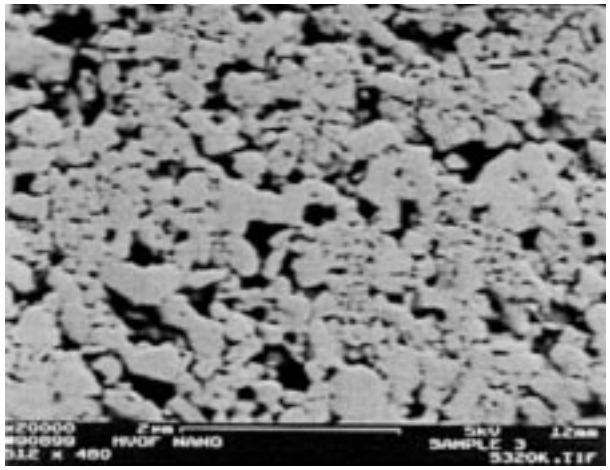

(a)

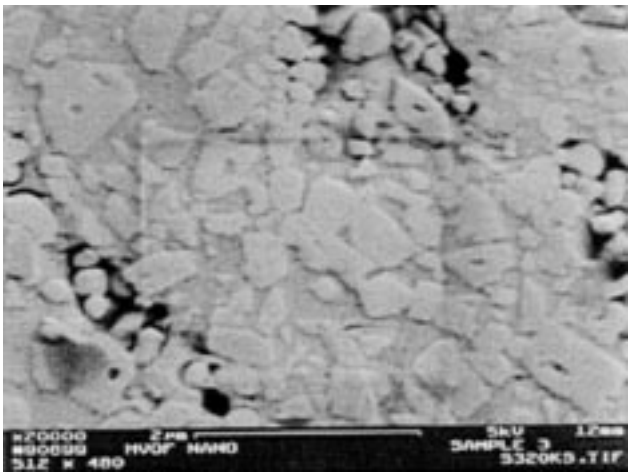

(b)

Fig. 3 SEM micrographs of the banded structure shown in Fig. 2, showing (**a**) extensive microporosity in the speckled band (**A**) and (**b**) the absence of such porosity in the clear band (**B**). Both bands show the presence of a fine distribution of WC particles, but they appear to be coarser in the pore-free band of the microstructure

substrate. In contrast, the heated but not melted part of that same particle should retain at least some, if not all, of its original microporosity. In agreement with this model, the hardness in the clear regions was 1050 ± 150 VHN, whereas that in the speckled regions was only 650 ± 35 VHN—the latter reflecting "softening" of the region by virtue of the presence of a fine distribution of micropores. In other words, despite a relatively uniform distribution of WC particles, the presence of microporosity substantially reduces the measured hardness of the coating, as would be expected.

If the temperature of any region of a heated particle exceeds the melting temperature of the WC-Co eutectic,[6] rapid dissolution of the WC nanoparticles in the liquid Co should occur, because of the high surface area of contact between the two nanophases. Thus, the amount of liquid Co, and its enrichment in W and C, should both increase with degree of superheat above the eutectic. Such an effect explains the observed variations in WC particle size and distribution in the clear regions of the microstructure, as noted above. It also provides an explanation for rapid oxidation and/or gasification of carbon during thermal spraying, because of the ease with which the dissolved carbon can diffuse through the liquid Co to react with the gaseous environment. Another consequence of the enrichment of liquid Co in W and C is that it should generate a high population density of strong tungsten/carbon clusters in the liquid phase, making it highly susceptible to amorphization during subsequent rapid solidification. Because the Co-rich liquid experiences splat quenching on the chilled substrate, it seems inevitable, therefore, that an amorphous Co-rich matrix phase will be developed, as in fact has been reported in the literature.[8,9] On the other hand, if the quenching rate is not high enough, then crystallization of mixed-metal carbide nanophases is to be expected. Evidence for η-carbide formation on an ultrafine scale has been found in x-ray diffraction patterns of some of the coatings (Fig. 6).

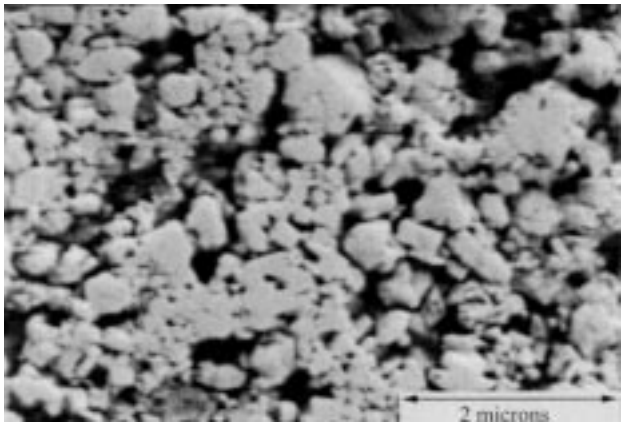

(a)

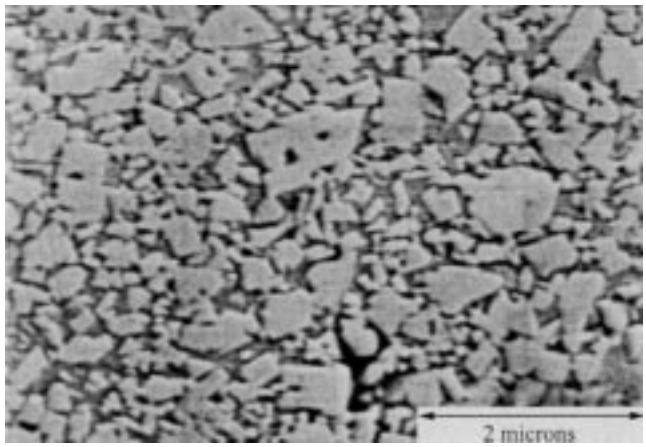

(b)

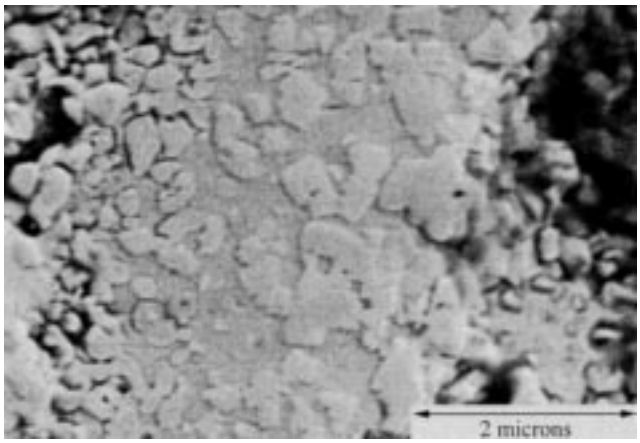

(c)

Fig. 4 Representative SEM micrographs of HVOF-sprayed WC/12 Co nanocoating, showing variations in WC particle size, shape, and degree of agglomeration, and associated nano-/microporosity: (**a**) region of incomplete densification, (**b**) region of nearly complete densification, and (**c**) region of superheated material, where the volume fraction of WC particles is reduced

X-ray diffraction patterns of the two types of coatings show that decarburization is more pronounced in the nanocoating material than in the microcoating material, (Fig. 6). The most prominent feature in the diffraction pattern of the nanocoating material is the evidence for W_2C and W phases, which account for about 27% of the total carbide content in the material. This behavior is considered to be a consequence of two related effects. First, formation of W_2C and W phases by reaction of WC nanoparticles with impurity oxygen in the HVOF environment. This includes oxygen and moisture in the feed gases, on the surfaces of the passivated nanoparticles, and as a result of mixing of ambient air with the combustion flame. Second, dissolution of WC particles in the liquid Co at high temperature, accompanied by C gasification and the formation of W_2C and/or W phases, as will be shown later. The latter effect depends on the degree of superheat experienced by the heterogeneously melted nanostructured particles.

The high surface area of the nanocomposite WC/Co particles facilitates all types of high-temperature reactions, which makes it difficult to establish one mechanism over another as being *primarily* responsible for the greater degree of decarburization encountered in the nanocoating case. However, exposure of the heterogeneously melted shell-like particles to localized superheating, leading to WC particle dissolution and decomposition, is considered to be an important mechanism accompanying oxidative reactions. Table 2 shows that carbon loss in the HVOF-derived nanostructured coating (1.37%) is about four times that of the conventional coating. Apparently, in this case, the higher surface of the nanostructured powder, together with its heterogeneous melting behavior, facilitates loss of carbon by oxidative reactions.

Because of the significance of the microstructural features discussed above, coating samples from various sources were examined. Without exception, all HVOF-derived nanocoatings showed a heterogeneous microstructure, similar to that of Fig. 2. However, different samples showed different amounts of interband porosity and relative volume fractions of speckled (microporous) and clear (dense) regions. This is taken to be evidence of the importance of controlling all aspects of HVOF deposition to generate nanocoatings with reproducible microstructures, properties, and performance. A particularly useful investigation would be to compare the effects of different size fractions of nanopowder feeds under identical HVOF spray conditions. Finer particles should experience more uniform melting characteristics and eliminate the patchy porosity described above. The resulting denser coating should possess higher hardness and, therefore, superior wear resistance.

The observations on the HVOF-deposited microcoatings were similar to that reported in the literature.[10] The most significant feature was the relatively uniform distribution of coarse WC particles in the Co matrix phase. An important difference was the absence of significant dissolution of WC particles in the liquid Co because of the low surface area of contact between the two phases. Another factor was the relatively low enrichment of the Co phase in W and C in the starting powder relative to that of the nanopowder, which is enriched in W and C by virtue of the chemical route used in its production.

3.2 Coatings Produced by APS Deposition

To gain further insight into the decarburization phenomenon, additional tests were performed using Ar/He and N_2/H_2 APS systems.

X-ray diffraction patterns showed evidence for extensive decarburization in the APS-deposited coatings, but the effect was

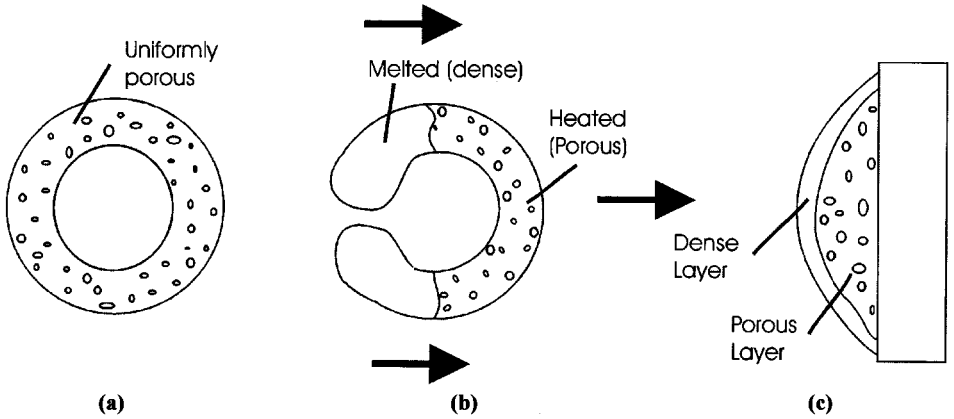

Fig. 5 Schematic representation of the formation of a banded coating structure when a partially melted and densified nano-WC/Co particle impacts on the substrate surface

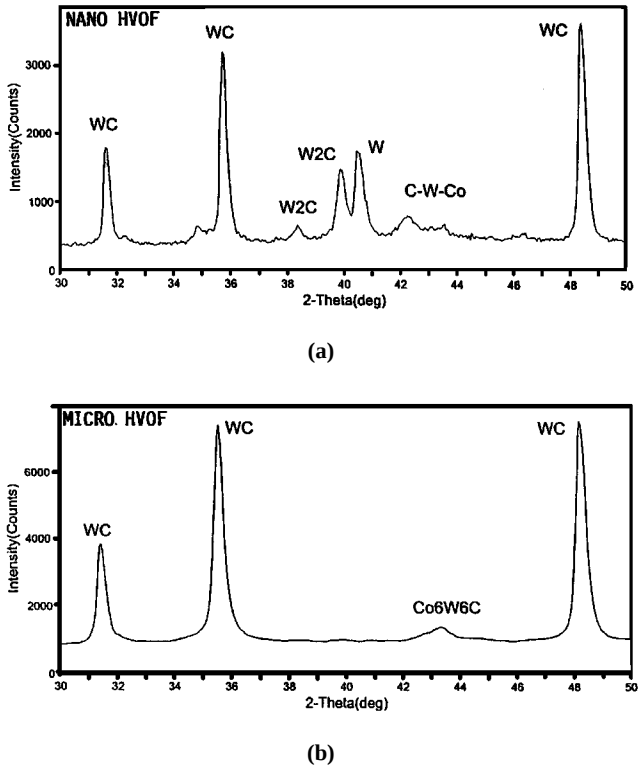

Fig. 6 X-ray diffraction patterns of HVOF-deposited WC/12Co coatings, showing evidence for more decarburization in the nanocoating sample (**a**) relative to the microcoating sample (**b**)

more pronounced in microcoatings than in nanocoatings (Fig. 7), which was the opposite of that found for HVOF-deposited coatings (Fig. 6). The sequence of phase changes was strikingly different in the two cases. In the microcoating case, decarburization involved the formation of W_2C and W at the expense of WC. However, the major phase was W_2C in the Ar/He plasma coating and W in the N_2/H_2 plasma coating. In contrast, in the nanocoating case, decarburization to form W_2C and W was not as pronounced.

Chemical analysis of HVOF and N_2/H_2 plasma coatings confirmed the trend in decarburization indicated by the x-ray analysis. Moreover, there was clear evidence for a major loss of Co, which was quite remarkable in the microcoating case. As shown in Table 2, the amount of Co decreases from 15 wt.% in the starting powder to 0.55 wt.% in the N_2/H_2 plasma coating, and there is a corresponding decrease in carbon content from 5.19 to 1.28 wt.%. Similar losses of Co and C occurred in the nanocoating case, but not as much as that in the microcoating case.

The microstructure of a N_2/H_2 plasma coating was quite different from that of an HVOF coating, irrespective of the type of powder feed used, *i.e.*, nanopowder versus micropowder. This was most clearly seen in a comparison of etched samples of the nanocoating material. The HVOF coating showed the presence of WC particles, (Fig. 8a), whereas there was little or no evidence for such particles in the N_2/H_2 plasma coating (Fig. 8b). The latter is consistent with Fig. 7, which shows that the major phases are W and W_2C, with only a small amount of residual WC phase due to extensive decarburization. Similar observations were made for the microcoating material, except that banding of the microstructure was more pronounced. The microstructures of the corresponding Ar/He plasma coatings more closely resembled the HVOF coatings than the N_2/H_2 plasma coatings, particularly in the nanocoating case, again consistent with the x-ray data (Fig. 7).

Hardness tests performed on both nano- and microcoatings showed consistently higher values for HVOF coatings relative to N_2/H_2 plasma coatings, reflecting the more extensive decarburization experienced in plasma spraying. Moreover, there was little difference in hardness between transverse and in-plane sections of the microstructure, despite the presence of microstructural banding.

4. Conclusions

Under HVOF spraying conditions, the extent of decarburization observed in the nanocoating material is greater than that in the microcoating material (Fig. 6). This effect has been seen repeatedly and appears to be independent of the type of HVOF

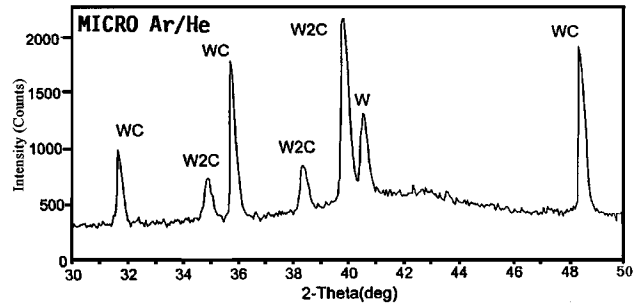

(a)

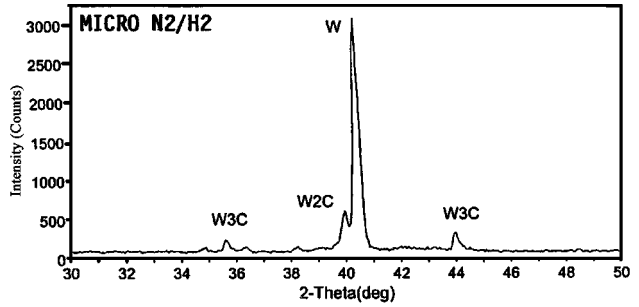

(b)

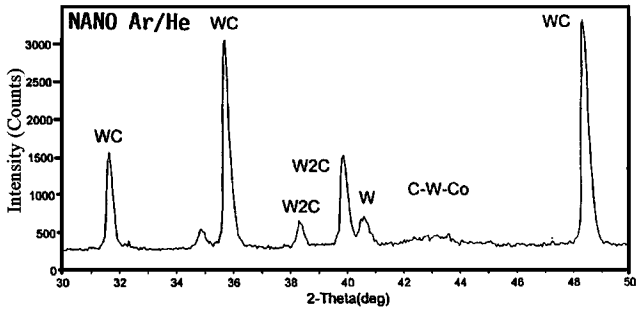

(c)

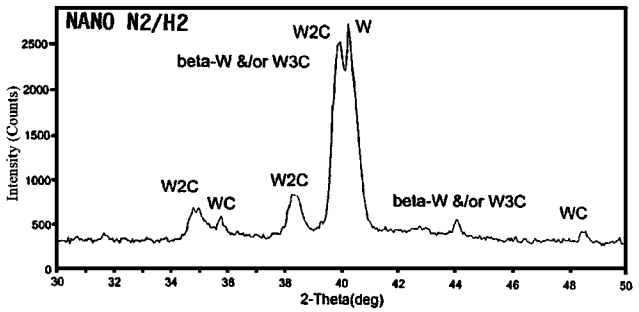

(d)

Fig. 7 X-ray diffraction patterns of APS-deposited WC/12Co coatings, showing evidence for more extensive decarburization in the microcoating samples (**a**) and (**b**) relative to the nanocoating samples (**c**) and (**d**)

spray parameters used. This leaves the source of the problem being the powder feed. As shown in Table 2, the impurity content in as-produced and oxygen-passivated powder from Nanodyne is about 1000 ppm. This alone is insufficient to account for

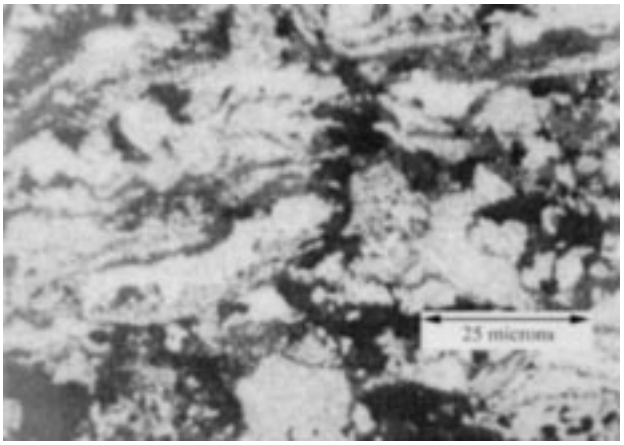

(a)

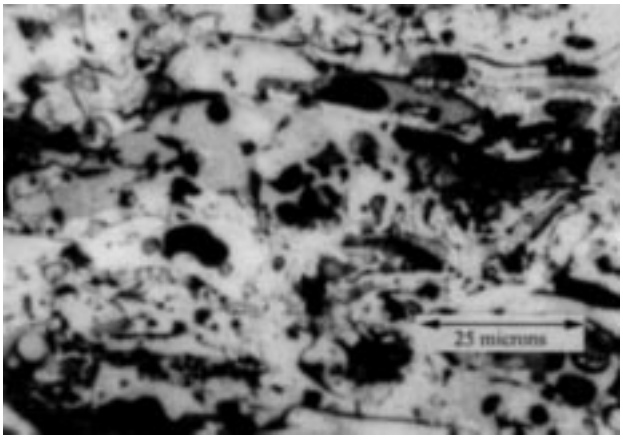

(b)

Fig. 8 Optical micrographs of WC/12Co nanocoating samples, comparing microstructures (etched condition) of (**a**) HVOF coating and (**b**) N_2/H_2 plasma coating. Note uniform distribution of fine WC particles in (a) and the absence of WC particles in (b), due to extensive decarburization in the N_2/H_2 plasma coating

the formation of W_2C and W phases by selective oxidation of WC nanoparticles. Handling of the fragile, shell-like particles, however, can easily cause fracture, exposing them to further oxidation. Again, exposure of even passivated nanopowder to humid air can result in chemisorption of water vapor, which renders the powder particles tacky and, therefore, difficult to feed. Thus, there are many sources of oxygen/water vapor contamination of the high-surface-area powder, which can contribute to decarburization during spraying. An interesting question is how these oxygen-rich contaminants affect decarburization within the banded structure of the HVOF nanocoating. Clearly, both regions are susceptible to decarburization, but visible evidence by SEM for W_2C and W phases is lacking. Further high-resolution analytical electron microscopy work is needed to resolve this question.

The much higher average particle temperature realized during plasma spraying, relative to HVOF spraying, causes more

extensive decarburization. A surprising result is the almost complete decarburization of the microcoating material using a N_2/H_2 plasma, as well as the gross loss of Co. Evidently, in this case, particle temperatures are so high that vaporization of Co and C occurs to an unusual degree, even during the very short residence times of the particles in the hot zone of the plasma. The reduced susceptibility of the nanocoating to these compositional changes is probably a reflection of the lowering of the vapor pressure of the liquid Co because of its enrichment in W and C. The mechanism of C gasification needs further investigation, but it could be enhanced by reactions with the ionized gas species in the plasma.

Taking all these factors into consideration, the following picture emerges of the compositional and structural changes occurring during thermal spraying of WC/Co particles (Fig. 9). As the initial Co-coated WC particle is heated above the melting point of the WC-Co eutectic (~1350 °C), the WC core of the particle undergoes dissolution in the liquid Co. Because the liquidus curve rises steeply on the WC-rich side of the eutectic, the volume fraction of the liquid Co phase increases with temperature, whereas that of the solid WC phase decreases. At the same time, carbon rapidly diffuses through the liquid Co and gasifies at the particle surface, *e.g.*, by the oxidative reaction $2C + O_2 \rightarrow 2CO$. With high degrees of superheat above the eutectic, as in plasma spraying, Co and C also evaporate from the particle surface. During subsequent cooldown from the superheated state (and possibly at the peak temperature), the Co-rich liquid becomes supersaturated, resulting in the formation of W_2C and/or W phases, depending on the extent of Co and C loss (decarburization) experienced by the original WC/Co particle. Here, it is presumed that the remaining WC core of the semisolid particle acts as a favorable site for nucleation and growth of coarse grains of W_2C and/or W phases. Finally, after further cooling below the eutectic temperature, fine-scale precipitation of η-carbide phases, such as W_3Co_3C and W_6Co_6C, may occur in the Co-rich matrix, due to a reduction in solid solubility with decreasing temperature. A possible example of this phenomenon is shown in Fig. 10.

In agreement with observations, Fig. 9 anticipates that the extent of decarburization should be sensitive to both surface area and morphology of the WC/Co powder feed particle. Thus, a shell-like WC/Co nanocomposite particle should be particularly

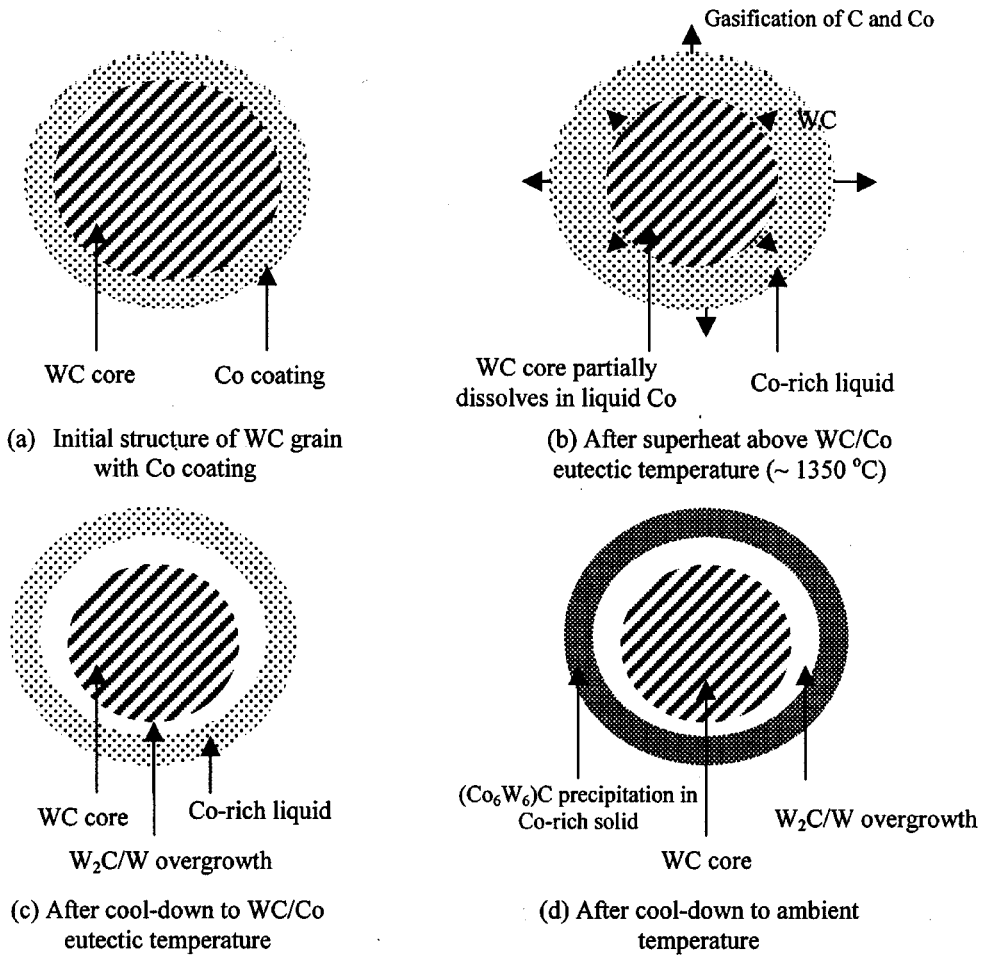

Fig. 9 Schematic representation of the proposed sequence of events leading to decarburization of thermal sprayed WC/Co powder, accompanied by the formation of W_2C and/or W phases

susceptible to decarburization for two reasons. First, the high surface area of the porous particle enables rapid reaction with the gaseous environment, particularly with any oxygen or water vapor trapped within the particles. Second, heterogeneous melting and localized superheating experienced by the shell-like particle (Fig. 5) due to poor heat transfer through the highly porous medium enables extensive dissolution of WC particles in the liquid Co, thereby providing the means for C gasification by rapid diffusion through liquid Co. Under the same conditions, a conventional WC/Co powder particle should not be as susceptible to decarburization, because of the lower surface area contact between the micron-sized WC and Co phases (hence more sluggish solution kinetics for WC in liquid Co) and the more uniform heating and melting of the much denser particles (hence reduced superheat of the particles).

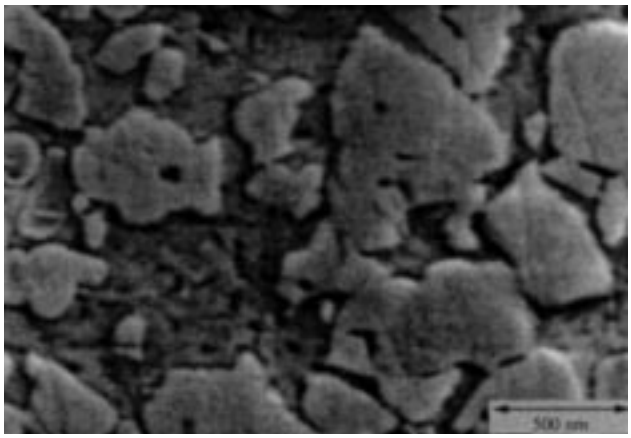

(a)

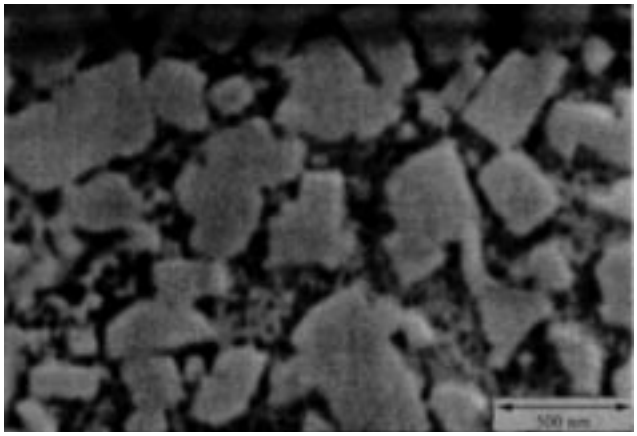

(b)

Fig. 10 Evidence for fine-scale precipitation (possibly η-carbide phases) in the Co-rich matrix phase of an HVOF-derived nanocoating: (**a**) high superheat showing absence of microporosity and reduced volume fraction of WC phase and (**b**) low superheat showing some residual microporosity and high volume fraction of WC phase. Note fine-scale precipitation in the Co-rich matrix phase due to the presence of η-carbide phases

To reduce the extent of decarburization encountered in HVOF spraying of WC/Co nanopowder, therefore, one approach is to densify the feed particles prior to spraying. This can be done by annealing the as-produced and passivated powder at high temperatures so as to eliminate any impurity oxygen and/or water vapor present in the material and to avoid decarburization during the annealing treatment. Perhaps the ideal starting structure for the nanophase material would be similar to that shown in Fig. 4(b), where particle densification has been accomplished without significant coarsening of the WC grains. The heat treatment required to accomplish this objective is being investigated. Another approach is to minimize the amount of oxygen species in the flame by using a lean fuel-oxygen mixture.

In summary, therefore, differences in behavior of conventional and nanostructured WC/Co powders during HVOF spraying are a consequence of intrinsic differences in their structure and morphology. In particular, heterogeneous melting and localized superheating of the high-surface-area nanopowder is considered to be the controlling factor in decarburization. The situation is further complicated in APS deposition by high-temperature vaporization of Co and C.

Acknowledgments

Support from the Office of Naval Research (Contract Nos. N00014-97-1-0249, N00014-97-1-0844, and N00014-98-3-0005) is gratefully acknowledged.

References

1. H. Gleiter: *Progr. Mater. Sci.,* 1989, vol. 33 (4), p 223.
2. R.W. Siegel: *Mater. Sci. Eng. A: Struct. Mater.: Prop., Microstr. Processing,* 1993, No. 2, p 189-97.
3. B.H. Kear and P. Strutt: *KONA Powder Particle,* 1995, No. 13, p 45-55.
4. L.E. McCandlish, B.H. Kear, and J. Bhatia: U.S. Patent 5,352,269, 1994.
5. L.E. McCandlish, B.H. Kear, and B.K. Kim: *Mater. Sci. Technol.,* 1990, vol. 6, p 953.
6. *ASM Handbook,* ASM, Materials Park, OH, 1992, vol. 3, p 2.115.
7. R.M. German: *Liquid Phase Sintering,* Plenum Press, New York, NY, 1985.
8. L.E. McCandlish, B.H. Kear, B.K. Kim, and L.Wu: in *Protective Coatings: Processing and Characterization,* R.M. Yazici, ed., TMS, Warrendale, PA, 1990, p 113-43.
9. C.J. Li, A. Ohmori, and Y. Harada: *J. Thermal Spray Technol.,* 1996, vol. 5, (1), p 69-73.
10. H.L. de Villiers Lovelock: *J. Thermal Spray Technol.,* 1998, vol. 7 (3), p 357-73.